J. Fluid Mech. (2022), *vol*. 946, A24, doi:10.1017/jfm.2022.601

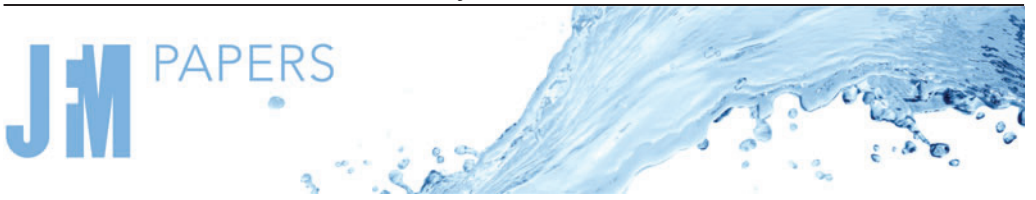

Numerical investigation of the effect of surface viscosity on droplet breakup and relaxation under axisymmetric extensional flow

Natasha Singh[1] **and Vivek Narsimhan**[1],†

[1]Davidson School of Chemical Engineering, Purdue University, 480 Stadium Mall Drive, West Lafayette, IN 47907, USA

(Received 5 January 2022; revised 26 June 2022; accepted 4 July 2022)

In this study, we perform boundary-integral simulations to investigate the role of interfacial viscosity in the deformation and breakup of a single droplet suspended in an axisymmetric extensional flow under the Stokes flow regime. We model the insoluble surfactant monolayer using the Boussinesq–Scriven constitutive relationship for a Newtonian interface. We compare the deformation and breakup results from our boundary-element simulations with results from small deformation perturbation theories. We observe that the surface shear/dilational viscosity increases/decreases the critical capillary number beyond which the droplet becomes unstable and breaks apart by reducing/increasing the droplet deformation at a given capillary number compared with a clean droplet. We present the relative importance of surface shear and dilational viscosity on droplet stability based on their measured values reported in experimental studies on surfactants, lipid bilayers and proteins. In the second half of the paper, we incorporate the effect of surfactant transport by solving the time-dependent convection–diffusion equation and consider a nonlinear equation of state (Langmuir adsorption isotherm) to correlate the interfacial tension with the changes in surfactant concentration. We explore the coupled influence of pressure-dependent surface viscosity and Marangoni stresses on droplet deformation and breakup. In the case of a droplet with pressure-dependent surface shear viscosity, we find that a droplet with pressure-thinning/thickening surfactant is less/more deformed than a droplet with pressure-independent surfactant. We conclude by discussing the combined impact of surface viscosity and surfactant transport on the relaxation of an initially extended droplet in a quiescent external fluid.

Key words: breakup/coalescence, boundary integral methods

† Email address for correspondence: vnarsim@purdue.edu

1. Introduction

Understanding the deformation and breakup of a droplet in a viscous flow plays an essential role in designing stable emulsions and foams for diverse industrial applications (Langevin 2000; Dan *et al.* 2013; van Kempen *et al.* 2013; Lam, Velikov & Velev 2014; Hamed, Schenck & Fiegel 2020). Droplet breakup analysis can guide the generation of dispersed-phase droplets with a size distribution aptly tuned for chemical reactors, droplet microencapsulation, inkjet printing and spraying systems (Frankel & Acrivos 1970; Kennedy, Pozrikidis & Skalak 1994; Belyaeva *et al.* 2004; Lemenand *et al.* 2013; Daly *et al.* 2015; Narsimhan, Wang & Xiang 2019; He *et al.* 2017). There is extensive research on the deformation and breakup of a clean droplet under different domains of external flow types. Barthes-Biesel & Acrivos (1973) first developed perturbation theories for examining the critical conditions for the breakup of a droplet under a general linear flow field in the limit of small droplet deformations. Some theoretical studies have examined the deformation and breakup of long slender droplets in shear and extensional flows where the internal fluid has a very low viscosity compared with the suspending fluid (Acrivos & Lo 1978; Hinch & Acrivos 1979, 1980). Some studies have experimentally investigated the transient effects in the deformation and burst of viscous droplets (Bentley & Leal 1986; Stone, Bentley & Leal 1986). Rallison & Acrivos (1978) and Rallison (1981) have numerically explored the deformation and breakup of a viscous droplet in extensional and shear flows.

The role of simple surfactants in the deformation and breakup of droplets has also been widely investigated. Here, the role of surfactants is to change the surface tension of the interface as well as introduce Marangoni flows (Stone & Leal 1990; Milliken, Stone & Leal 1993; Pawar & Stebe 1996; Li & Pozrikidis 1997; Vlahovska, Bławzdziewicz & Loewenberg 2009; Kamat *et al.* 2018). Some studies have also focused on the deformation and burst of elastic capsules in extensional and simple shear flows using theories and experiments (Li, Barthes-Biesel & Helmy 1988; Chang & Olbricht 1993). The mechanical behaviour of artificial capsules and vesicles and their different modelling strategies are reviewed in Barthès-Biesel (2009).

Suspensions of droplets and bubbles laden with lipid bilayers, polymers, proteins and solid particles exhibit complex interfacial rheology. The interplay among surface viscoelastic effects, Marangoni stresses, surface pressure changes, surfactant solubility and diffusivity governs the mechanics of these complex interfaces (Jaensson, Anderson & Vermant 2021; Pourali *et al.* 2021). The role of interfacial rheology in droplet mechanics remains underexplored. Droplet interfaces embedded with certain low-molecular-weight surfactants (eicosanol, hexadecanol) and proteins (β-casein) form highly viscous membranes (Brooks *et al.* 1999; Fuller & Vermant 2012; Gunning *et al.* 2013; Verwijlen, Moldenaers & Vermant 2013). In such systems, the in-plane friction that arises when the molecules/particles within the interface slide past each other results in viscous dissipation, i.e. interfacial viscosities. The surface rheology of viscous interfaces can be modelled using the Boussinesq–Scriven law that provides an expression for the interfacial traction that arises from the surface shear and dilational viscosities (Boussinesq 1913; Scriven 1960). Erni (2011) reviews the influence of interfacial viscosity in the shear and dilational modes of deformation in systems with complex interfaces. Several experimental studies have also explored the different techniques to measure the interfacial shear and dilational rheological properties of complex fluid interfaces (Miller *et al.* 2010; Choi *et al.* 2011; Fuller & Vermant 2012; Balemans, Hulsen & Anderson 2016; Jaensson *et al.* 2021).

In recent years there have been advances in understanding the effect of surface rheology on droplet deformation and breakup using theories and numerical simulations.

Flumerfelt (1980) first examined the impact of surface viscosities on droplet deformation in shear and extensional flows by extending the first-order perturbation analysis developed in Cox (1969) for a clean droplet. Narsimhan (2019) developed second-order perturbation theories to describe the shape and rheology of a droplet with interfacial shear and dilational viscosity. The condition for the breakup of a droplet with surface viscosity in a linear flow field is presented in Singh & Narsimhan (2020) in the limit of small droplet deformation. The deformation and breakup of a droplet in shear flow using boundary-element simulations have been explored in Gounley *et al.* (2016) and Luo, Shang & Bai (2019). Herrada *et al.* (2022) also examined the steady-state solutions and stability of a gaseous droplet with interfacial viscosity using linear stability analysis and numerical computations in extensional flow. These previous studies have shown that the surface shear viscosity reduces the droplet deformation and increases the critical capillary number for droplet breakup compared with a clean droplet at the same viscosity ratio. In contrast, surface dilational viscosity enhances the droplet deformation and reduces the critical capillary number for droplet breakup compared with a clean droplet at the same viscosity ratio. In this work, we perform boundary-element simulations to investigate the role of surface viscosity in droplet deformation and breakup under axisymmetric extensional flow for a wide range of viscosity ratio values, interfacial viscosity and surfactant parameters. We present the mechanism behind the effect of surface shear and dilational viscosity on droplet deformation using traction arguments from interfacial viscosities. We also explore the combined impact of surface viscosity and surfactant transport on droplet relaxation in a quiescent fluid for different viscosity contrasts between the inner and outer fluid and surfactant transport parameters. We compare the results from our numerical simulations with those of second-order analytical theories in the limit of small capillary number (Narsimhan 2019; Singh & Narsimhan 2020). Numerical investigation of this problem allows us to examine stronger deformations, the effects of Marangoni stresses and the effects of pressure-thickening/thinning surface viscosities, the latter of which have not been addressed in previous studies.

2. Problem set-up and methodology

2.1. *Problem overview*

We numerically investigate how interfacial rheology alters the dynamics of a droplet suspended in an unbounded immiscible fluid and subject to an external flow. Figure 1 shows a schematic of the problem. We consider an initially spherical droplet of radius R' placed in a uniaxial extensional flow symmetric about the z' axis. We model the problem in polar-cylindrical coordinates with origin at the centre of the droplet. The internal fluid viscosity is $\lambda\eta'$, and the external fluid viscosity is η'. The interface of the droplet has an insoluble monolayer of a surface-active agent. We assume that the surfactant monolayer is primarily viscous. In this work, we neglect surface elasticity effects and employ the Boussinesq–Scriven constitutive relationship to describe the rheology of the viscous Newtonian interface (Boussinesq 1913; Scriven 1960). The surfactant interface has a surface shear viscosity η'_μ, a surface dilational viscosity η'_κ and a surface tension σ'. As the droplet deforms under external flow, the flow around the droplet can affect the local surface tension σ', surfactant concentration Γ' and surface viscosity (η'_κ and η'_μ) on the interface. We discuss the formulations of variable surface tension and surface viscosity in the next subsection.

The steady-state deformation of the droplet under flow is characterized by the Taylor deformation parameter $D_{Taylor} = (L' - B')/(L' + B')$, where L' and B' are the lengths of

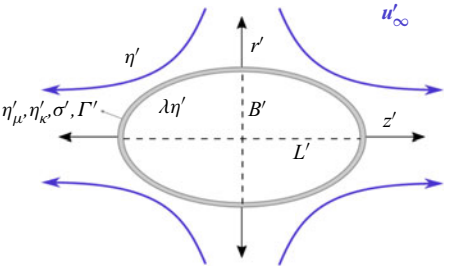

Figure 1. Problem overview.

the major and minor axes, respectively, as shown in figure 1. The undisturbed far-field velocity vector $\boldsymbol{u}'_\infty$ in dimensional form is expressed as

$$\boldsymbol{u}'_\infty = G' \cdot \begin{bmatrix} -1 & 0 & 0 \\ 0 & -1 & 0 \\ 0 & 0 & 2 \end{bmatrix} \cdot \boldsymbol{x}'. \tag{2.1}$$

In the above equation, G' represents the external strain rate and $\boldsymbol{x}'$ represents the position vector. Throughout the paper, primed variables are in dimensional form while unprimed variables are in dimensionless form.

2.2. *Governing equations*

We non-dimensionalize all lengths by radius R' of the initial spherical droplet, viscosities by the outer fluid viscosity η', times by the inverse strain rate G'^{-1}, velocities by $G'R'$, bulk stresses by $\eta' G'$ and surface stresses by $R'\eta' G'$. The interfacial surfactant concentration and surface tension are normalized by their initial equilibrium values Γ'_{eq} and σ'_{eq} at time $t = 0$.

The fluid flow inside and outside of the droplet is described by the Stokes and continuity equations. The dimensionless forms of these equations are

$$\lambda \nabla^2 \boldsymbol{u}^{in} = \nabla p^{in}, \quad \nabla \cdot \boldsymbol{u}^{in} = 0, \tag{2.2a}$$

$$\nabla^2 \boldsymbol{u}^{out} = \nabla p^{out}, \quad \nabla \cdot \boldsymbol{u}^{out} = 0. \tag{2.2b}$$

The boundary conditions at the interface are as follows.

(i) Continuity of velocity:

$$\boldsymbol{u}^{in} = \boldsymbol{u}^{out} = \boldsymbol{u}_s, \tag{2.3}$$

where $\boldsymbol{u}_s$ represents the velocity of the interface.

(ii) Force balance:

$$(\boldsymbol{\tau}^{in} - \boldsymbol{\tau}^{out}) \cdot \boldsymbol{n} = \boldsymbol{f}_\mu + \boldsymbol{f}_\kappa + \frac{1}{Ca} (\nabla_s \sigma - \sigma \boldsymbol{n} \nabla \cdot \boldsymbol{n}). \tag{2.4}$$

In (2.4), $\boldsymbol{\tau}^{in} - \boldsymbol{\tau}^{out}$ is the traction jump across the interface, $Ca = G'\eta' R'/\sigma'_{eq}$ represents the capillary number, σ is the dimensionless surface tension and $\boldsymbol{n}$ is the outward-pointing normal. The expressions for the interfacial shear traction $\boldsymbol{f}_\mu$ and the interfacial dilational

traction $\boldsymbol{f}_{\kappa}$ in (2.4) are given by the Boussinesq–Scriven constitutive relationship (Boussinesq 1913; Scriven 1960):

$$\boldsymbol{f}_{\kappa} = \nabla_s \cdot [Bq_{\kappa} \boldsymbol{P}(\nabla_s \cdot \boldsymbol{u}_s)], \tag{2.5}$$

$$\boldsymbol{f}_{\mu} = -\nabla_s \cdot [Bq_{\mu} \boldsymbol{P}(\nabla_s \cdot \boldsymbol{u}_s) - \boldsymbol{P} \cdot (\nabla_s \boldsymbol{u}_s + \nabla_s \boldsymbol{u}_s{}^T) \cdot \boldsymbol{P}]. \tag{2.6}$$

In the above expressions, $\boldsymbol{P} = \boldsymbol{I} - \boldsymbol{nn}$ is the projection operator on the surface, $\nabla_s = \boldsymbol{P} \cdot \nabla$ is the surface gradient, $Bq_{\mu} = \eta'_{\mu}/R'\eta'$ is the Boussinesq number for the surface shear viscosity and $Bq_{\kappa} = \eta'_{\kappa}/R'\eta'$ is the Boussinesq number for the surface dilational viscosity.

As an alternative way of quantifying the surface viscous effects, we introduce additional dimensionless parameters $Bq = Bq_{\mu} + Bq_{\kappa}$ and interfacial viscosity ratio $\lambda_{ds} = \eta'_{\kappa}/\eta'_{\mu}$. The former represents the ratio of combined interfacial forces to the bulk viscous forces, while the latter represents the relative ratio of surface dilational to shear viscosity.

The changes in surfactant concentration Γ along the droplet's surface are taken into account using the time-dependent convection–diffusion equation (Stone 1990; Wong, Rumschitzki & Maldarelli 1996):

$$\frac{\partial \Gamma}{\partial t} + \nabla_s \cdot (\Gamma \boldsymbol{u}_t) + \Gamma(\nabla_s \cdot \boldsymbol{n})(\boldsymbol{u}_s \cdot \boldsymbol{n}) = \frac{1}{Pe_s} \nabla_s^2 \Gamma, \tag{2.7}$$

where $Pe_s = CaR'\sigma'_{eq}/D'_s\eta'$ is the surface Péclet number, $\boldsymbol{u}_t$ is the tangential component of the interfacial velocity $\boldsymbol{u}_s$ and D'_s is the surface diffusivity of the surfactant molecules. The surface Péclet number is the ratio of surface convection rate to the surface diffusion rate of the surfactant. In (2.7), the interpretation of the time derivative is such that the surface coordinates are fixed. In our numerical code, we displace the grid points in the direction normal to the interface. Therefore, the term $-\dot{\boldsymbol{x}} \cdot \nabla_s \Gamma$ (that arises because of the displacement of the grid points along the surface as the droplet deforms) is zero in the evolution equation given by Wong *et al.* (1996).

We consider the Langmuir equation of state to relate the surface tension to the surfactant concentration at the interface:

$$\sigma = \frac{\sigma'_c}{\sigma'_{eq}} + E \ln\left(1 - \frac{\Gamma}{\Gamma_{\infty}}\right). \tag{2.8}$$

In the above equation, σ'_c is the surface tension of a clean interface without surfactant. The dimensionless parameter $E = R'_G T' \Gamma'_{\infty}/\sigma'_{eq}$ is the surface elasticity number, where R'_G is the ideal gas constant, T' is the absolute temperature and Γ'_{∞} is the maximum packing density for a given surfactant system.

At initial time $t = 0$, we assume a homogeneous distribution of surfactant over the interface of the droplet ($\Gamma = 1$) and (2.8) can be rewritten as

$$\sigma = 1 + E \ln\left(\frac{\Gamma_{\infty} - \Gamma}{\Gamma_{\infty} - 1}\right). \tag{2.9}$$

In the case of non-homogeneous distribution of surfactant over the droplet's surface, the surface viscosities can vary strongly with surface pressure $\Pi' = \sigma'_c - \sigma'$, as has been explored in several experimental studies (Kurtz, Lange & Fuller 2006; Kim *et al.* 2011; Fuller & Vermant 2012; Kim *et al.* 2013; Samaniuk & Vermant 2014). The dependence of

surface viscosity on surface tension is taken into account using the following expressions (Manikantan & Squires 2017):

$$\eta_{\kappa}'^{\pm} = \eta_{\kappa,eq}' \exp\left(\pm \frac{\Pi' - \Pi_{eq}'}{\Pi_c'}\right), \tag{2.10}$$

$$\eta_{\mu}'^{\pm} = \eta_{\mu,eq}' \exp\left(\pm \frac{\Pi' - \Pi_{eq}'}{\Pi_c'}\right), \tag{2.11}$$

where $+$ and $-$ signs represent a pressure-thickening and pressure-thinning surfactant, respectively; $\eta_{\mu,eq}'$ and $\eta_{\kappa,eq}'$ denote the equilibrium shear and dilational surface viscosity at the initial value of surface pressure Π_{eq}'; and Π_c' is the pressure scale over which significant surface viscosity changes occur (Manikantan & Squires 2017).

The dimensionless forms of (2.10) and (2.11) are

$$Bq_{\kappa}^{\pm} = Bq_{\kappa,eq} \exp\left(\pm \frac{1-\sigma}{\Pi_c}\right), \tag{2.12}$$

$$Bq_{\mu}^{\pm} = Bq_{\mu,eq} \exp\left(\pm \frac{1-\sigma}{\Pi_c}\right). \tag{2.13}$$

In the above equations, $\Pi_c = \Pi_c'/\sigma_{eq}'$ is the dimensionless surface pressure scale.

The dimensionless parameters are summarized in table 1. The ranges of surface parameters (Bq_{μ}, Bq_{κ}, Π_c, E) explored in this study are based on their experimental values reported in previous literature (Brooks *et al.* 1999; Kurtz *et al.* 2006; Georgieva *et al.* 2009; Kim *et al.* 2011; Fuller & Vermant 2012; Kim *et al.* 2013; Verwijlen *et al.* 2013; Hermans & Vermant 2014; Samaniuk & Vermant 2014; Zell *et al.* 2014; Manikantan & Squires 2017; Singh & Narsimhan 2021). The surface Péclet number is based on surface diffusivity measurements listed in Shmyrov & Mizev (2019) that are collected from various sources. The surface diffusivity can vary widely depending on the phase behaviour of the adsorbed surfactant. A rule of thumb is that many macroscopic droplets (millimetre or above) will have $Pe_s \gg 1$ while those that are small (e.g. nanoemulsions or microemulsions) will have $Pe_s \sim O(1)$ or smaller.

2.3. *Numerical implementation and validation*

We implement axisymmetric boundary-element simulations to numerically compute the droplet's interfacial velocity. The velocity at the interfacial location $\boldsymbol{x_0}$ can be expressed as

$$\boldsymbol{u_s}(\boldsymbol{x_0}) = -\frac{1}{4\pi(1+\lambda)} \int_C \boldsymbol{M}(\boldsymbol{x}, \boldsymbol{x_0}) \cdot [[\boldsymbol{\tau} \cdot \boldsymbol{n}]] \, \mathrm{d}l(\boldsymbol{x}) + \frac{1}{4\pi} \frac{1-\lambda}{1+\lambda} \int_C^{PV} \boldsymbol{q}(\boldsymbol{x}, \boldsymbol{x_0}) \cdot \boldsymbol{u_s}(\boldsymbol{x}) \, \mathrm{d}l(\boldsymbol{x}). \tag{2.14}$$

In the above equation, $\boldsymbol{M}$ and $\boldsymbol{q}$ represent the single-layer and the double-layer potentials (Pozrikidis 1990, 1992), $[[\boldsymbol{\tau} \cdot \boldsymbol{n}]]$ is the traction jump across the interface and $\mathrm{d}l$ is the differential arclength along the droplet contour.

The droplet surface is discretized into N elements connecting $N+1$ nodes. The detailed numerical implementation to solve the boundary-integral equation (2.14) and the convection–diffusion equation (2.7) can be found in the axisymmetric code developed

λ	Viscosity ratio	$\lambda = \dfrac{\text{Inner fluid viscosity}}{\text{Outer fluid viscosity}}$	$0.01 \leqslant \lambda \leqslant 10$
Ca	Capillary number	$Ca = \dfrac{G'\eta' R'}{\sigma'_{eq}}$	$0 \leqslant Ca \leqslant 0.2$
Bq_μ	Boussinesq parameter for surface shear viscosity	$Bq_\mu = \dfrac{\eta'_\mu}{R'\eta'}$	$0 \leqslant Bq_\mu \leqslant 10$
Bq_κ	Boussinesq parameter for surface dilational viscosity	$Bq_\kappa = \dfrac{\eta'_\kappa}{R'\eta'}$	$0 \leqslant Bq_\kappa \leqslant 10$
Bq	Boussinesq parameter for total surface viscosity	$Bq = \dfrac{\eta'_\kappa + \eta'_\mu}{R'\eta'}$	$0 \leqslant Bq \leqslant 10$
λ_{ds}	Interfacial viscosity ratio	$\lambda_{ds} = \dfrac{\eta'_\kappa}{\eta'_\mu}$	$0 \leqslant \lambda_{ds} < \infty$
Π_c	Surface pressure scale	$\Pi_c = \dfrac{\Pi'_c}{\sigma'_{eq}}$	$\Pi_c = \{0.1, 0.25\}$
Pe_s	Surface Péclet number	$Pe_s = \dfrac{CaR'\sigma'_{eq}}{D'_s\eta'}$	$0.01 \leqslant Pe_s \leqslant 1000$
E	Surface elasticity number	$E = \dfrac{R'_G T' \Gamma'_\infty}{\sigma_{eq}}$	$E = \{0.2, 0.4, 2\}$
Γ_∞^{-1}	Initial surfactant coverage	$\Gamma_\infty^{-1} = \dfrac{\Gamma'_{eq}}{\Gamma'_\infty}$	$\Gamma_\infty^{-1} = 0.5$

Table 1. Dimensionless parameters.

in Singh & Narsimhan (2021). A typical simulation starts with $N = 100$ nodes on a spherical droplet interface. The time step Δt is set as $(2\text{–}6) \times 10^{-3} Ca$ to update the droplet shape using the numerical scheme and the re-meshing procedure described in Singh & Narsimhan (2021). To ensure that the total surfactant is conserved on the droplet's surface, we rescale the surfactant concentration at each time step. Therefore, the surfactant concentration integrated over the interface is constant over time. In the absence of such rescaling, we find that the error in total surfactant concentration integrated over the interface is less than 0.6 % for the simulations shown in the paper. The droplet is considered to have attained a steady-state deformation when the interfacial normal velocity $|\boldsymbol{u_n}| < 0.01$ at all collocation points. The critical capillary number Ca_C denotes the largest value of Ca below which the droplet attains a steady-state deformation under flow.

To validate our code, we compare our results with boundary-element simulations from Pawar & Stebe (1996). Figure 2 shows the variation of Taylor deformation parameter D_{Taylor} with capillary number Ca for a clean droplet with viscosity ratio $\lambda = 1$. In the same plot, we also compare our numerical results with those of second-order perturbation theories developed in previous studies (Barthes-Biesel & Acrivos 1973; Vlahovska *et al.* 2009; Narsimhan 2019; Singh & Narsimhan 2020) and the lowest-order perturbation analysis from Flumerfelt (1980). The lowest-order perturbation theories solve the droplet shape up to $O(Ca)$ for $Ca \ll 1$, while the second-order theories solve the shape up to $O(Ca^2)$ (Barthes-Biesel & Acrivos 1973; Vlahovska *et al.* 2009; Narsimhan 2019). At $O(Ca)$, the analytical expression of the Taylor deformation parameter for a droplet with surface shear and dilational viscosity under uniaxial extensional flow is given as (Taylor 1934; Flumerfelt 1980)

$$D_{Taylor} = \frac{15}{32} \frac{19\lambda + 16 + 24Bq_\kappa + 8Bq_\mu}{5\lambda + 6Bq_\kappa + 4Bq_\mu + 5} Ca. \tag{2.15}$$

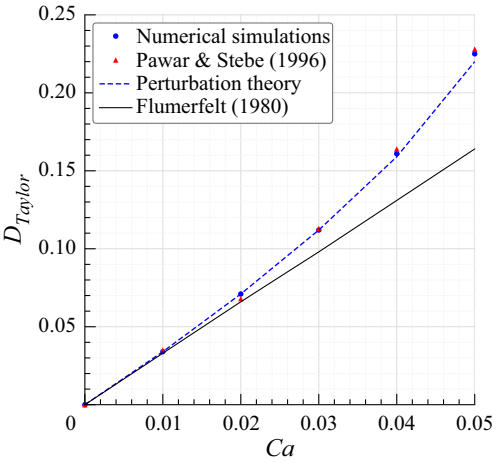

Figure 2. Plot of D_{Taylor} versus Ca for a clean droplet without surfactant and viscosity ratio $\lambda = 1.0$. The blue dots represent our numerical results and the red triangles represent boundary-element simulations from Pawar & Stebe (1996). The dashed blue curve is from second-order perturbation analysis (Barthes-Biesel & Acrivos 1973; Vlahovska *et al.* 2009; Singh & Narsimhan 2020), and the black solid curve is the lowest-order perturbation analysis from Flumerfelt (1980).

Our results compare well with the numerical simulation from Pawar & Stebe (1996) and the second-order perturbation theories at all Ca values. At $Ca > 0.01$, we see that the lowest-order perturbation analysis shows deviations from the data predicted from simulations and underpredicts the D_{Taylor} values.

3. Results: droplet deformation and breakup

In §§ 3.1–3.3, we explore the effect of surface viscosity and surfactant transport on the deformation and breakup of a droplet placed in an extensional flow.

3.1. *Comparison with small deformation perturbation theories for constant surface viscosity*

In this section, we discuss the effect of constant surface viscosity on the steady-state deformation and the critical capillary number Ca_C for droplet breakup. This analysis assumes that surface tension is constant and that surfactant is homogeneously distributed on the interface. Surfactant transport effects are neglected to analyse the isolated impact of interfacial viscosity on droplet dynamics. Sections 3.2 and 3.3 examine the coupling between interfacial viscosity, Marangoni stresses and surface dilution.

Figure 3 shows the variation of D_{Taylor} with $Bq = Bq_\kappa + Bq_\mu$ for a droplet with interfacial viscosity ratio $\lambda_{ds} = Bq_\kappa/Bq_\mu = 1$. We observe that at a given capillary number, the steady-state deformation D_{Taylor} of the droplet decreases upon increasing Bq. Our numerical results compare well with those of the small deformation perturbation theories at $O(Ca^2)$ (Narsimhan 2019; Singh & Narsimhan 2020). Again, we see that the lowest-order perturbation analysis using (2.15) underpredicts the D_{Taylor} values, and this effect is more significant at $Ca = 0.05$ than at $Ca = 0.01$.

Figure 4 shows the variation of D_{Taylor} with interfacial viscosity ratio λ_{ds} for a droplet with viscosity ratio $\lambda = 1$, $Ca = 0.05$ at Bq values of 2, 5 and 10. Ratio $\lambda_{ds} = 0$ represents a droplet with pure surface shear viscosity, and $\lambda_{ds} = \infty$ represents a droplet with pure

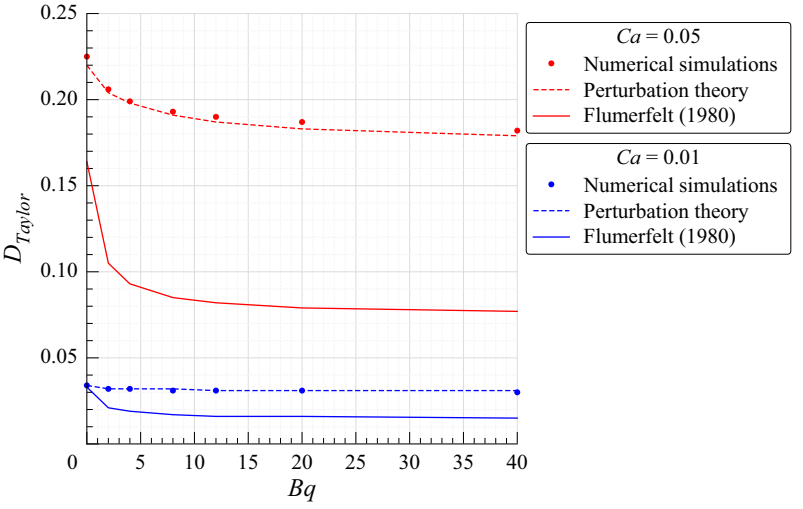

Figure 3. Plots of D_{Taylor} versus Bq for a droplet with interfacial viscosity ratio $\lambda_{ds} = 1$ at capillary number values 0.01 and 0.05. The dots represent our numerical results, dashed curves are from second-order perturbation theories (Narsimhan 2019; Singh & Narsimhan 2020) and bold curves are from using first-order perturbation theory (2.15).

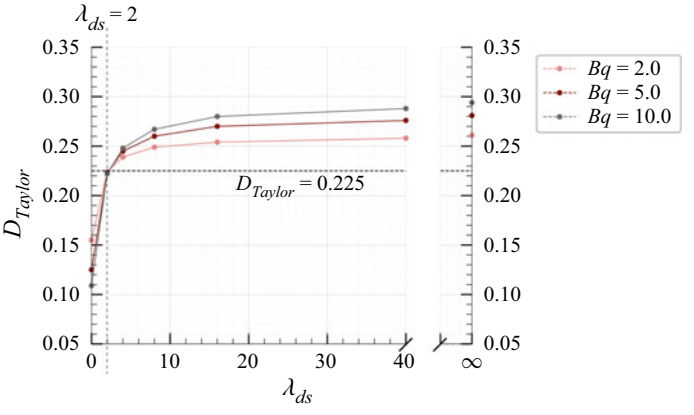

Figure 4. Plots of D_{Taylor} versus λ_{ds} for a droplet with viscosity ratio $\lambda = 1$, $Ca = 0.05$ and Bq values of 2, 5 and 10. Here D_{Taylor} for a clean droplet without surfactant at $Ca = 0.05$ and $\lambda = 1$ is shown using a horizontal black dashed line.

surface dilational viscosity. The horizontal dashed line shows D_{Taylor} for a clean droplet without surfactant at $Ca = 0.05$ and $\lambda = 1$. We observe that at $\lambda_{ds} \approx 2.0$, D_{Taylor} of a droplet with surface viscosity is the same as that of a clean droplet for different Bq values. Droplets with λ_{ds} below this critical value exhibit smaller deformations than a clean droplet, and the deformation decreases as the interfacial effects (Bq) increase. Droplets with λ_{ds} above the critical value demonstrate the opposite effect – i.e. they exhibit larger deformations than clean droplets, and the deformation increases as the interfacial effects (Bq) increase. We observe qualitatively similar behaviour if we examine droplets at different viscosity ratios λ. The critical λ_{ds} where the droplet deformation is the same as that for a clean droplet shifts to $\lambda_{ds} = 0.9$ for a droplet with viscosity ratio $\lambda = 0.1$

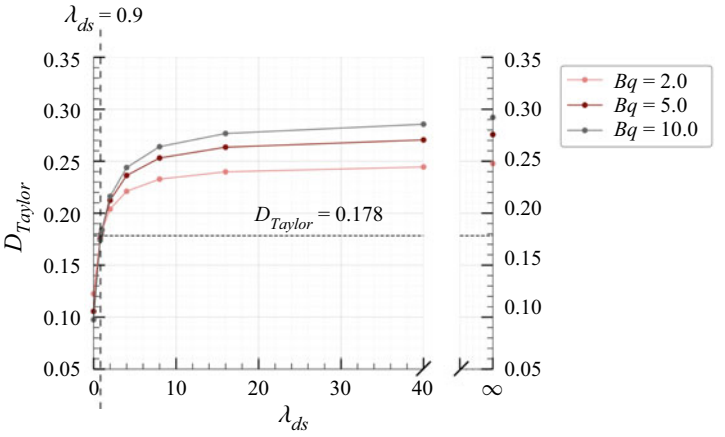

Figure 5. Plots of D_{Taylor} versus λ_{ds} for a droplet with viscosity ratio $\lambda = 0.1$, $Ca = 0.05$ and at Bq values of 2, 5 and 10. Here D_{Taylor} for a clean droplet without surfactant at $Ca = 0.05$ and $\lambda = 0.1$ is shown using a horizontal black dashed line.

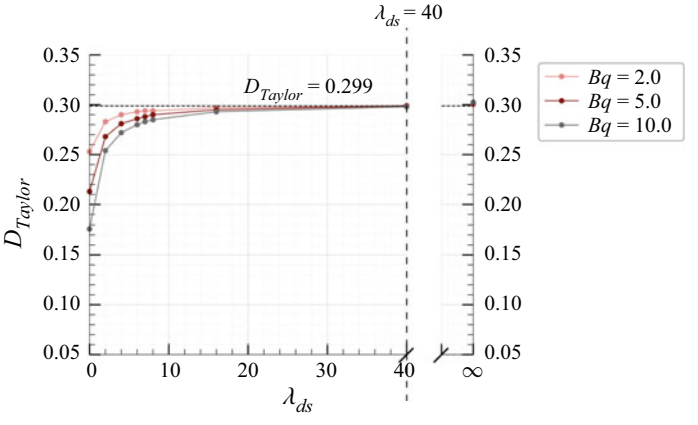

Figure 6. Plots of D_{Taylor} versus λ_{ds} for a droplet with viscosity ratio $\lambda = 10$, $Ca = 0.05$ and at Bq values of 2, 5 and 10. Here D_{Taylor} for a clean droplet without surfactant at $Ca = 0.05$ and $\lambda = 10$ is shown using a horizontal black dashed line.

(see figure 5), while the critical value shifts to $\lambda_{ds} = 40$ for a droplet with viscosity ratio $\lambda = 10$ (see figure 6).

The experimentally reported values of surface dilational viscosity are found to be much larger than surface shear viscosity as $\lambda_{ds} > O(1)$ for most interfacial monolayers. For instance, the interfacial viscosity ratio estimates of lipid monolayer dipalmitoylphosphatidylcholine and dimyristoylphosphatidylethanolamine are reported to be $\lambda_{ds} \sim O(10^5)$ (Krägel *et al.* 1996; Kim *et al.* 2011). Surface rheological studies of various interfacial monolayers have shown $\lambda_{ds} \sim O(10^3)$ for poly(*t*-butyl methacrylate) system (Krägel *et al.* 1996; Samaniuk & Vermant 2014), $\lambda_{ds} \sim O(10^4)$ for hexadecanol interface (Verwijlen *et al.* 2013; Samaniuk & Vermant 2014), $\lambda_{ds} \sim O(1)$ for protein β-casein monolayer (Freer *et al.* 2004; Erni, Windhab & Fischer 2011) and $\lambda_{ds} \sim O(10^6)$ for viscoelastic globular protein ovalbumin interface (Erni *et al.* 2003; Xiong *et al.* 2018). The results shown in figures 4, 5 and 6 suggest that the combined influence of surface

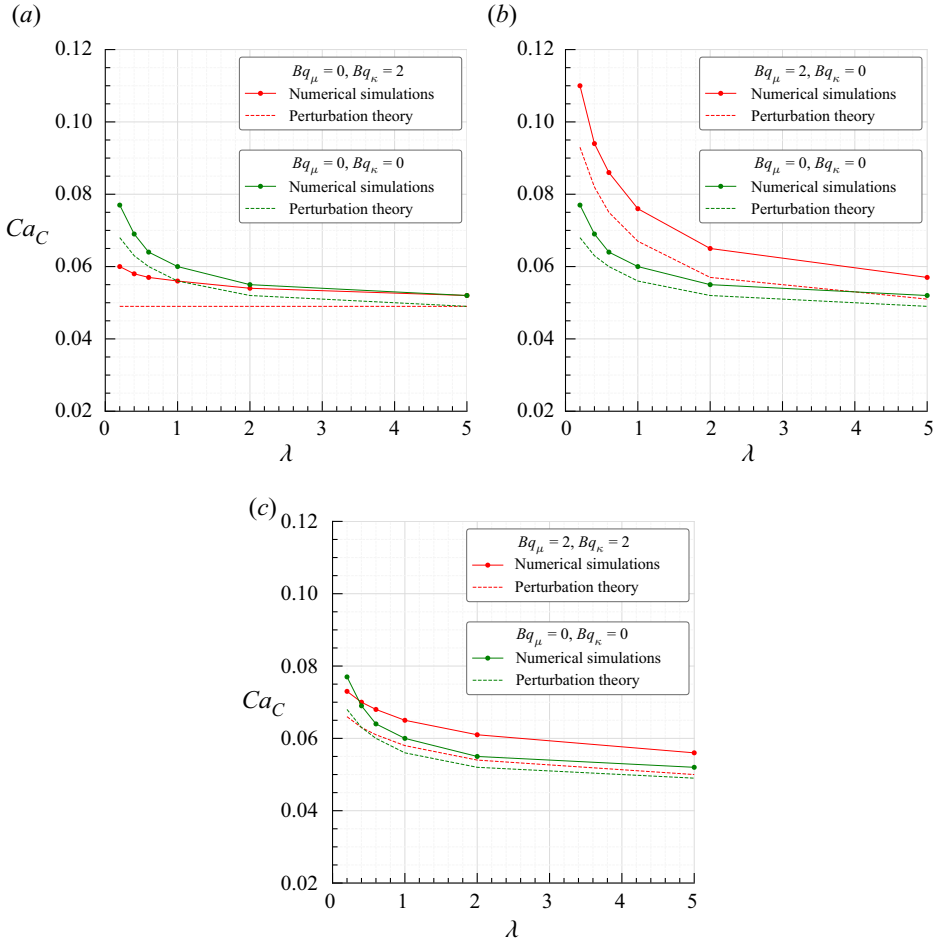

Figure 7. Critical capillary number Ca_C versus viscosity ratio λ for a clean droplet and a droplet with surface viscosity. The solid lines correspond to boundary-element simulations, while the dashed lines correspond to second-order perturbation theories (Narsimhan 2019; Singh & Narsimhan 2020). (*a*) Effect of surface dilational viscosity. (*b*) Effect of surface shear viscosity. (*c*) Effect of equal surface shear and dilational viscosity.

shear and dilational viscosity will increase the droplet deformation compared with a clean droplet at the same capillary number for most surfactant systems.

The next part of this section examines how interfacial viscosity alters the critical capillary number Ca_C for drop breakup. The critical capillary number Ca_C is defined as the largest value of Ca below which the droplet will attain a steady-state deformation under flow ($|\boldsymbol{u_n}| < 0.01$ at all collocation points). Above this capillary number, the droplet will keep deforming and become unstable. Figure 7 compares the variation of Ca_C with viscosity ratio λ from the small deformation theories (represented by dashed lines) and numerical simulations (represented by bold lines). From figure 7(*a*), we can see that the surface dilational viscosity reduces Ca_C of the droplet compared with a clean droplet at the same viscosity ratio λ. When $\lambda > 4$, we observe that Ca_C of a droplet with dilational viscosity is nearly the same as Ca_C of a clean droplet from both theory and simulations. In contrast, we observe that the surface shear viscosity increases Ca_C compared with a clean droplet at the same λ (figure 7*b*). From figure 7(*c*), we can see the effect of equal surface

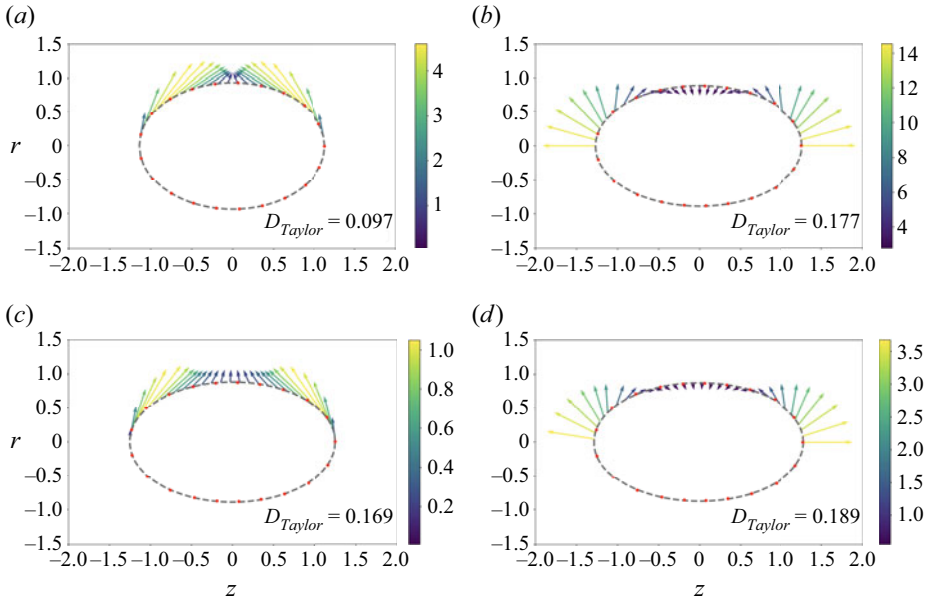

Figure 8. Steady-state droplet shapes at $Ca = 0.04$ for four different cases: (*a*) $Bq_\mu = 2, Bq_\kappa = 0$ and $\lambda = 0.1$; (*b*) $Bq_\mu = 0, Bq_\kappa = 2$ and $\lambda = 0.1$; (*c*) $Bq_\mu = 2, Bq_\kappa = 0$ and $\lambda = 10$; (*d*) $Bq_\mu = 0, Bq_\kappa = 2$ and $\lambda = 10$. Shapes drawn using red dots are from second-order perturbation theories (Narsimhan 2019) and shapes drawn with dashed lines are from boundary-element simulations. The vectors shown in the droplet's upper half represent the computed traction from interfacial viscosity (2.5) and (2.6). For a clean droplet, $D_{Taylor} = 0.137$ at $\lambda = 0.1$ and $D_{Taylor} = 0.187$ at $\lambda = 10$.

shear and dilational viscosities on Ca_C. In this case, the Ca_C values are lower than that of the clean droplet for viscosity ratio $\lambda < 0.4$ and are higher than that of the clean droplet for viscosity ratio $\lambda > 0.4$. The numerical results from boundary-element simulations are in good qualitative agreement with the small deformation theories for the three cases shown in figure 7. Previous studies examining clean droplets under extensional flow have also reported the Ca_C values from analytical theories to be within 15 % agreement with the numerical results (Rallison & Acrivos 1978), which is what we observe here.

Figure 8 shows steady-state droplet shapes at $Ca = 0.04$ for a droplet with pure surface shear viscosity $Bq_\mu = 2, Bq_\kappa = 0$ (figure 8*a*,*c*) and a droplet with pure surface dilational viscosity (figure 8*b*,*d*) at viscosity ratio values $\lambda = 0.1$ and $\lambda = 10$. The vectors shown in the droplet's upper half represent the computed traction from interfacial viscosity (2.5) and (2.6). As can be seen from figure 8, the droplet shapes from boundary-element simulations (drawn using dashed lines) match well with the droplet shapes from second-order perturbation theories (drawn using red dots). For a clean droplet, $D_{Taylor} = 0.137$ at $\lambda = 0.1$ and $D_{Taylor} = 0.187$ at $\lambda = 10$. In the case of a droplet with pure surface shear viscosity (figure 8*a*,*c*), the shear traction opposes the surface velocity gradients and reduces the droplet deformation compared with the clean droplet. For a droplet with pure dilational viscosity, the expression of dilational traction (2.5) mimics the formulation of variable surface tension. The influence of surface dilational viscosity can be seen as an 'effective' surface tension (Singh & Narsimhan 2021):

$$\sigma^{effective} = \sigma + Bq_\kappa(\nabla_s \cdot \boldsymbol{u}_s). \tag{3.1}$$

The negative divergence of velocity in the droplet's pole reduces the effective surface tension in the pole region, and we observe that the droplet with surface dilational viscosity

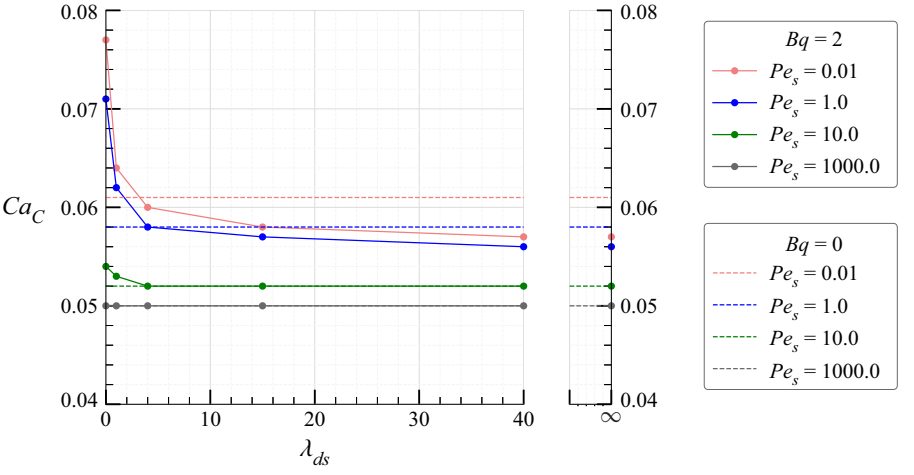

Figure 9. Variation of Ca_C with λ_{ds} for a droplet with $Bq = 2$ at Pe_s values 0.01, 1, 10 and 1000. The dashed horizontal lines denote Ca_C of the droplet in the absence of surface viscosity, i.e. $Bq = 0$. The dimensionless parameters are: $\lambda = 1$, $E = 0.2$ and $\Gamma_\infty^{-1} = 0.5$.

is more deformed than a clean droplet at the same Ca (figure 8*b*,*d*). The effect of surface dilational viscosity appears similar to the influence of surfactant convection. When a droplet is placed under extensional flow, the surfactant gets swept towards the droplet's pole. The higher surfactant concentration in the pole region reduces the effective surface tension and increases the droplet deformation (Pawar & Stebe 1996; Feigl *et al.* 2007).

From figure 8, we can see that the interfacial traction acting on the droplet's surface is more significant at $\lambda = 0.1$ than at $\lambda = 10$ for both surface shear and dilational viscosity (see scale for heat map). As a result, the surface viscosity influences the droplet deformation and Ca_C more strongly at lower values of viscosity ratio than higher values, as can be seen from figure 7.

3.2. *Combined influence of constant surface viscosity and surfactant transport*

As the droplet deforms under extensional flow, the surfactant can get swept from the droplet's equator towards the droplet's poles leading to non-homogeneous surfactant distribution. In this section, we include the effect of Marangoni stresses on droplet deformation and breakup, assuming the surface viscosity remains constant on the interface.

Figure 9 shows the variation of Ca_C with λ_{ds} for a droplet with $Bq = 2$ at surface Péclet number values 0.01, 1, 10 and 1000. The values of dimensionless parameters are: $\lambda = 1$, $E = 0.2$ and $\Gamma_\infty^{-1} = 0.5$. The dashed horizontal lines in the figure denote Ca_C of a droplet without surface viscosity, i.e. $Bq = 0$. We observe that the critical capillary number Ca_C decreases upon increasing λ_{ds} and approaches Ca_C of a droplet with pure surface dilational viscosity at $\lambda_{ds} = \infty$. The surface viscosity does not significantly impact droplet breakup at higher values of surface Péclet number ($Pe_s = 10$ and $Pe_s = 1000$). We find the Ca_C values for a droplet with interfacial viscosity to be the same as that without interfacial viscosity at $Pe_s = 1000$.

Figure 10(*a*) shows the droplet shapes at $Pe_s = 0.01$ and $Pe_s = 1000$ for a droplet with interfacial viscosity $Bq = 2$ and $\lambda_{ds} = 1$. The values of dimensionless parameters are: $Ca = 0.05$, $\lambda = 1$, $E = 0.4$ and $\Gamma_\infty^{-1} = 0.5$. The droplet at surface Péclet number

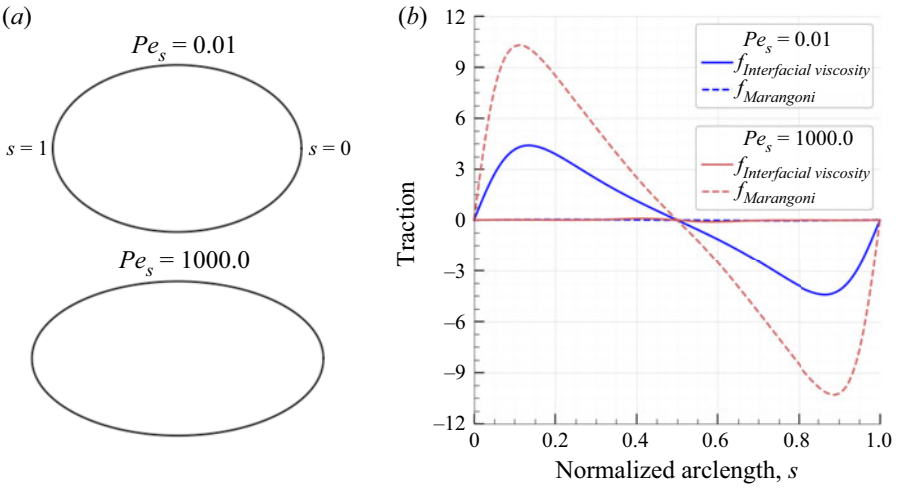

Figure 10. (*a*) Steady-state droplet shapes at $Pe_s = 0.01$ and $Pe_s = 1000$ for a droplet with $Bq = 2$ and $\lambda_{ds} = 1$. (*b*) Variation of tangential component of interfacial traction (shown by bold curves) and Marangoni traction (shown by dashed curves) with normalized arclength s for the droplet shapes shown in (*a*). The values of dimensionless parameters are: $Ca = 0.050$, $\lambda = 1$, $E = 0.4$ and $\Gamma_\infty^{-1} = 0.5$.

$Pe = 0.01$ appears less deformed than the droplet at $Pe = 1000$. Figure 10(*b*) shows the variation of tangential interfacial traction and Marangoni forces acting along the droplet's surface with normalized arclength s for the shapes shown in figure 10(*a*). At $Pe = 0.01$, we observe that the Marangoni effects are negligible compared with the surface viscosity effects. In contrast, at $Pe = 1000$, the traction contribution from interfacial viscosity is much smaller than the Marangoni forces. As a result, the interfacial viscosity has a negligible impact on droplet deformation and breakup at large Pe_s, and the Ca_C values approach the results for a droplet with only surfactant transport (as was observed in figure 9).

Figure 11 shows the variation of Ca_C with Bq for a droplet with equal surface shear and dilational viscosity $\lambda_{ds} = 1$. The values of dimensionless parameters are: $\lambda = 1$, $E = 0.2$ and $\Gamma_\infty^{-1} = 0.5$. Similar to the case of constant surface viscosity (figure 7*c*), for a droplet with surfactant transport, we observe that the droplet with equal interfacial viscosities has a higher Ca_C than that of a droplet without interfacial viscosity. We observe that increasing the interfacial viscosity has a higher impact on Ca_C at $Pe_s = 0.01$ than at $Pe_s = 10$. The interfacial viscosity has a negligible impact on Ca_C at $Pe_s = 1000$.

3.3. *Influence of pressure-dependent surface viscosity*

Previous literature has shown that the surface viscosity can change sharply with surface pressure (Kurtz *et al.* 2006; Kim *et al.* 2011; Fuller & Vermant 2012; Kim *et al.* 2013; Samaniuk & Vermant 2014). Here we discuss how the pressure-dependent surface shear and dilational viscosity enhance/reduce the droplet deformation and critical capillary number compared with the case of Π-independent surface viscosity. We include the effect of surfactant transport as in § 3.2, but now also let the surface viscosity vary with surfactant concentration.

We first discuss the impact of pressure-dependent surface shear viscosity on droplet deformation and breakup. Figure 12 shows the evolution of droplet shapes with time for a pressure-thinning surfactant with $\Pi_c = 0.25$ (shown in figure 12*a*) and a pressure-thickening surfactant with $\Pi_c = 0.25$ (shown in figure 12*b*) at capillary number

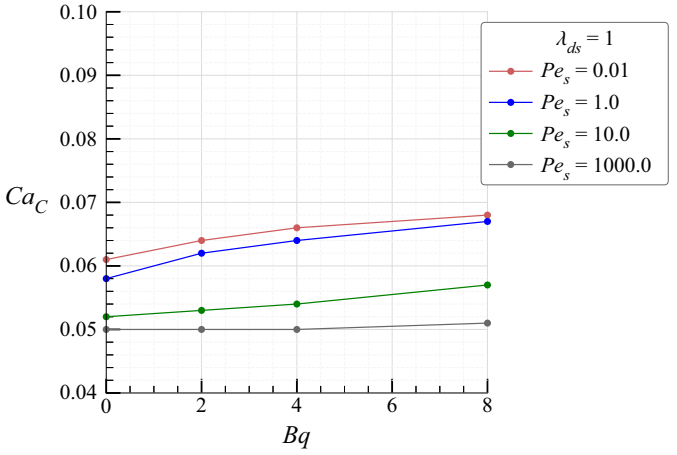

Figure 11. Variation of Ca_C with $Bq = Bq_\mu + Bq_\kappa$ for a droplet with interfacial viscosity ratio $\lambda_{ds} = 1$ at surface Péclet number values $Pe_s = 0.01$, 1, 10 and 1000. The values of dimensionless parameters are: $\lambda = 1$, $E = 0.2$ and $\Gamma_\infty = 2$.

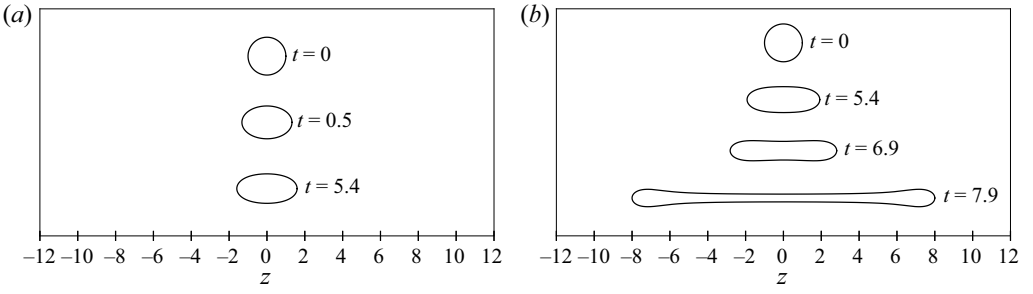

Figure 12. Time evolution of a droplet with pressure-dependent interfacial shear viscosity $Bq_{\mu,eq} = 2.0$: (*a*) $\Pi_c = 0.25$, pressure-thinning; (*b*) $\Pi_c = 0.25$, pressure-thickening. The values of dimensionless parameters are: $\lambda = 1$, $E = 0.4$, $\Gamma_\infty = 2$, $Ca = 0.08$ and $Pe_s = 0.01$.

$Ca = 0.08$. The values of dimensionless parameters are: $\lambda = 1$, $Pe_s = 0.01$, $E = 0.4$, $\Gamma_\infty = 2$, $Bq_{\mu,eq} = 2$ and $Bq_{\kappa,eq} = 0$. The droplet with Π-thinning surfactant eventually attains a stable shape under flow at time $t = 5.4$. In contrast, at the same capillary number, the droplet with Π-thickening surfactant deforms continuously with time and becomes unstable. In figure 13, we plot the variation of Bq_μ and surfactant concentration Γ with normalized arclength s ($s = 0$ and $s = 1$ at the droplet's two poles) for the droplet shapes shown in figures 12(*a*) and 12(*b*) at $t = 5.4$. At $Pe = 0.01$, the diffusion of the surfactant along the droplet's interface dominates over the surfactant convection. As a result, we observe a homogeneous distribution of surfactant on the droplet's surface and $\Gamma < 1$ over the entire droplet interface for Π-thickening and Π-thinning surfactant. The lowered surfactant concentration over the droplet's surface also lowers the droplet's Bq_μ for a Π-thickening surfactant and increases the droplet's Bq_μ for a Π-thinning surfactant. As a result, the droplet with Π-thinning surfactant breaks at a higher Ca than the droplet with Π-thickening surfactant. Tables 2 and 3 compare Ca_C of a droplet with a Π-thickening, Π-thinning and Π-independent surfactant at surface elasticity numbers $E = 0.4$ and $E = 2$, respectively.

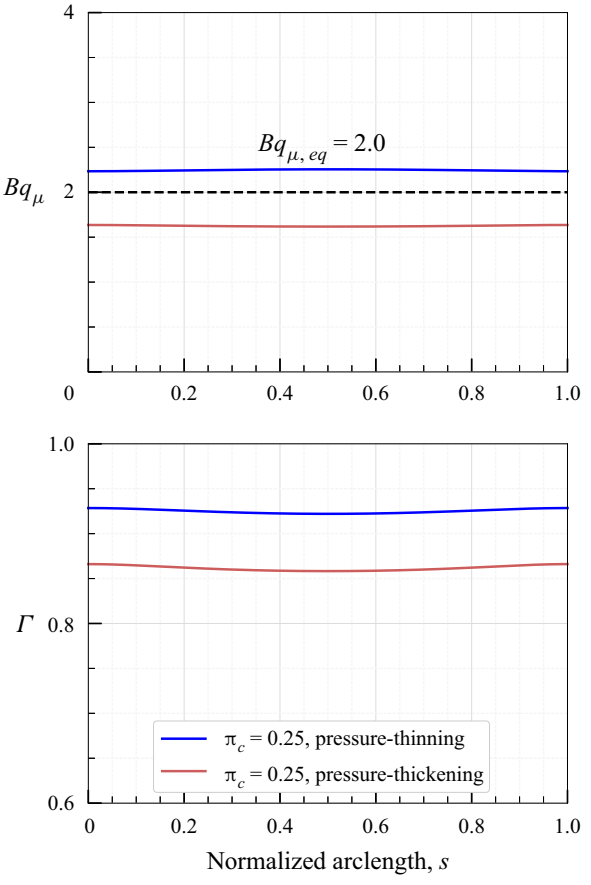

Figure 13. Variation of Bq_μ and surface concentration Γ with the normalized arclength s corresponding to the droplet shapes shown in figure 12 at time $t = 5.4$.

	Pressure-thinning ($\Pi_c = 0.1$)	Pressure-thinning ($\Pi_c = 0.25$)	Pressure-independent	Pressure-thickening ($\Pi_c = 0.25$)	Pressure-thickening ($\Pi_c = 0.1$)
$\lambda_{ds} = 0$	0.085	0.080	0.078	0.076	0.074
$\lambda_{ds} = \infty$	0.057	0.058	0.058	0.059	0.059

Table 2. Values of Ca_C of a droplet with $Bq_{eq} = 2$, $\lambda = 1.0$, $E = 0.4$, $\Gamma_\infty = 2$ and $Pe_s = 0.01$.

	Pressure-thinning ($\Pi_c = 0.5$)	Pressure-independent	Pressure-thickening ($\Pi_c = 0.5$)
$\lambda_{ds} = 0$	0.098	0.089	0.083
$\lambda_{ds} = \infty$	0.068	0.069	0.069

Table 3. Values of Ca_C of a droplet with $Bq_{eq} = 2$, $\lambda = 1.0$, $E = 2$, $\Gamma_\infty = 2$ and $Pe_s = 0.01$.

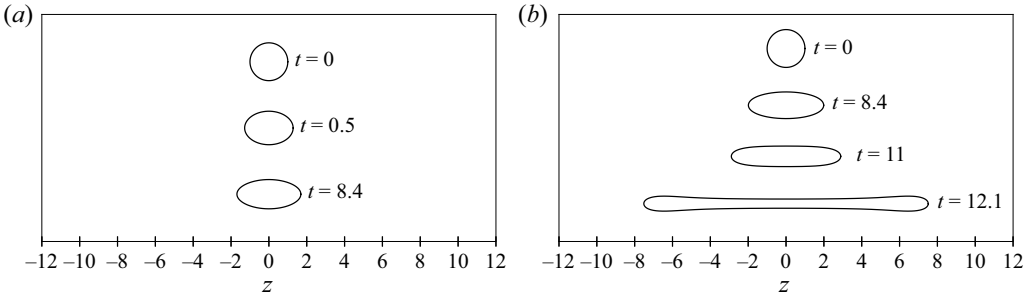

Figure 14. Time evolution of a droplet with pressure-dependent interfacial shear viscosity $Bq_{\mu,eq} = 2.0$: (*a*) $\Pi_c = 0.25$, pressure-thinning; (*b*) $\Pi_c = 0.25$, pressure-thickening. The values of dimensionless parameters are: $\lambda = 1$, $E = 0.4$, $\Gamma_\infty = 2$, $Ca = 0.056$ and $Pe_s = 10.0$.

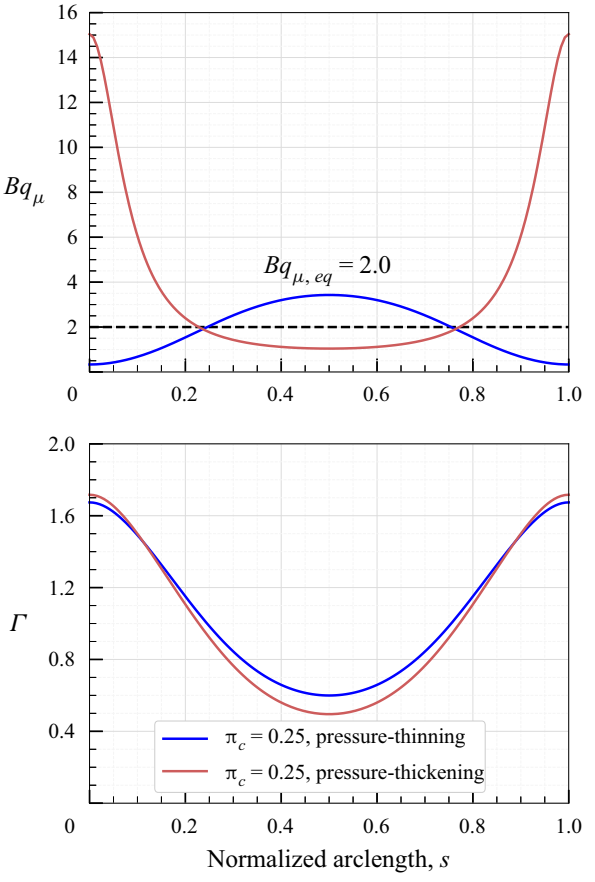

Figure 15. Variation of Bq_μ and surface concentration Γ with the normalized arclength s corresponding to the droplet shapes shown in figure 14 at time $t = 8.4$.

Figure 14 shows the evolution of droplet shapes with time for a pressure-thinning surfactant with $\Pi_c = 0.25$ (shown in figure 14*a*) and a pressure-thickening surfactant with $\Pi_c = 0.25$ (shown in figure 14*b*) at $Ca = 0.056$, but now the Péclet number is large ($Pe_s = 10$). Here also we observe that the droplet with Π-thinning surfactant attains a

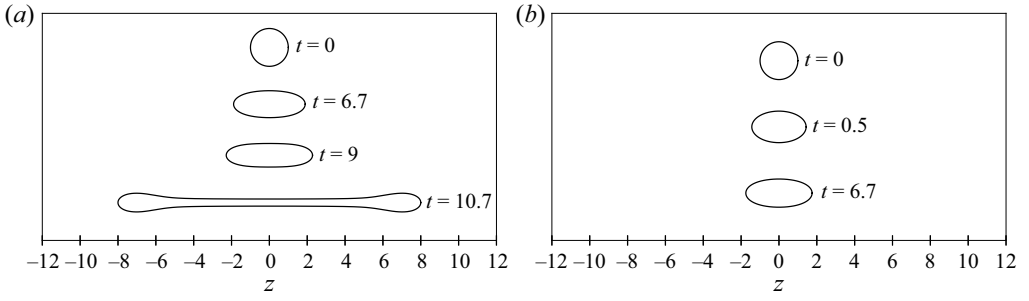

Figure 16. Time evolution of a droplet with pressure-dependent interfacial dilational viscosity $Bq_{\kappa,eq} = 2.0$: (*a*) $\Pi_c = 0.25$, pressure-thinning; (*b*) $\Pi_c = 0.25$, pressure-thickening. The values of dimensionless parameters are: $\lambda = 1$, $E = 0.4$, $\Gamma_\infty = 2$, $Ca = 0.059$ and $Pe_s = 0.01$.

stable shape under flow while the droplet with Π-thickening surfactant becomes unstable. Figure 15 shows the variation of Bq_μ and surfactant concentration Γ with normalized arclength s for the droplet shapes shown in figures 14(*a*) and 14(*b*) at $t = 8.4$. At $Pe_s = 10$, we observe that the surfactant gets convected towards the droplet's pole leading to $\Gamma > 1$ in the pole region and $\Gamma < 1$ in the equator region. The lowered surfactant concentration in the equator region for a droplet with Π-thinning surfactant increases the droplet's Bq_μ and surface shear traction acting on the droplet's equator. For a droplet with only surface shear viscosity, what matters is traction near the droplet's equator and not traction near the droplet's poles, as was discussed for figure 8. As a result, the droplet with pressure-thinning surfactant breaks at a larger Ca than the droplet with pressure-thickening surfactant (Ca_C of a droplet with pressure-thinning surfactant is 0.056, while Ca_C of a droplet with pressure-thickening surfactant is 0.054). We observe similar behaviour of pressure-dependent surface viscosity at a higher value of surface elasticity number. At $E = 2$, Ca_C of a droplet with pressure-thinning surfactant is 0.067, while Ca_C of a droplet with pressure-thickening surfactant is 0.064.

Next we discuss the impact of a Π-thickening and Π-thinning surfactant on a droplet with only surface dilational viscosity. Figure 16 shows the droplet shape evolution for a pressure-thinning and pressure-thickening surfactant (figure 16*a*,*b*). Unlike surface shear viscosity, here we see that the droplet with Π-thickening surfactant attains a stable shape and the droplet with Π-thinning surfactant becomes unstable. Here, for a droplet with Π-thickening surfactant, the lowered surfactant concentration due to strong diffusive effects lowers the droplet's Bq_κ and increases Ca_C compared with a Π-thinning surfactant. Table 2 compares Ca_C of a droplet with a Π-thickening, Π-thinning and Π-independent surfactant at $Pe_s = 0.01$. From table 2 we can see that the effects of Π-thickening and Π-thinning surfactant are not very pronounced for a droplet with only dilational viscosity compared to a droplet with only surface shear viscosity.

In the case of a droplet with only surface dilational viscosity at $Pe_s = 10$, we do not observe a difference in Ca_C for Π-thickening and Π-thinning surfactant. The convection of surfactant towards the droplet's pole at $Pe_s = 10$ increases/decreases the droplet's Bq_κ in the pole region for Π-thickening/thinning surfactant, and we observe the droplet with Π-thickening surfactant is slightly more deformed compared with the droplet with Π-thinning surfactant. Because we do not observe a significant difference in deformation at large Pe_s for a droplet with only surface dilational viscosity, the results for the Π-thickening and Π-thinning surfactant for this case are omitted in the paper.

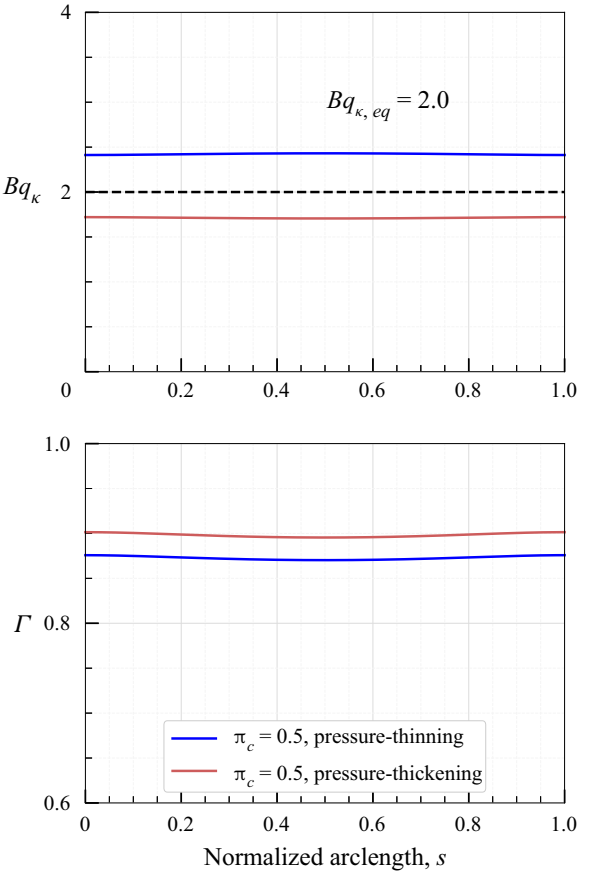

Figure 17. Variation of Bq_κ and surface concentration Γ with the normalized arclength s corresponding to the droplet shapes shown in figure 16 at time $t = 6.7$.

4. Results: droplet relaxation in quiescent fluid

In this section, we discuss the combined influence of surface viscosity and surfactant transport on the relaxation of an initially extended droplet in a quiescent flow. For the results presented in this section, a spherical droplet of radius R' at a given set of non-dimensional parameters is first stretched under extensional flow to a specified initial non-dimensional length $L = L'/R'$, where L' is the length of the droplet's major axis. The flow is then stopped to examine the relaxation of the extended droplet in the now quiescent external fluid.

In the absence of external flow, we non-dimensionalize all lengths by R', viscosities by the outer fluid viscosity η', velocities by σ'_{eq}/η', time by $R'\eta'/\sigma'_{eq}$, bulk stresses by σ'_{eq}/R' and surface stresses by σ'_{eq}. The interfacial surfactant concentration and surface tension are normalized by their equilibrium values Γ'_{eq} and σ'_{eq} on a spherical droplet of radius R' placed under no external flow.

The non-dimensionalized time-dependent convection–diffusion equation in the absence of flow can be written as

$$\frac{\partial \Gamma}{\partial t} + \nabla_s \cdot (\Gamma \boldsymbol{u_t}) + \Gamma(\nabla_s \cdot \boldsymbol{n})(\boldsymbol{u_s} \cdot \boldsymbol{n}) = \frac{1}{\gamma}\nabla_s^2 \Gamma. \tag{4.1}$$

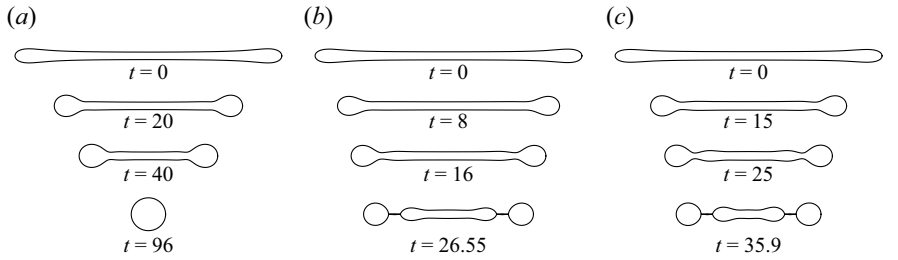

Figure 18. Relaxation of an initially extended droplet in a stagnant fluid for three cases having the same initial shape ($L = 16.0$) over time: (a) droplet with surface shear viscosity ($Bq_\mu = 1$, $Bq_\kappa = 0$), (b) clean droplet ($Bq_\mu = 0$, $Bq_\kappa = 0$) and (c) droplet with surface dilational viscosity ($Bq_\mu = 0$, $Bq_\kappa = 1$). The values of dimensionless parameters are: $\lambda = 1$, $E = 0.2$, $\Gamma_\infty = 2$ and $\gamma = 1.0$.

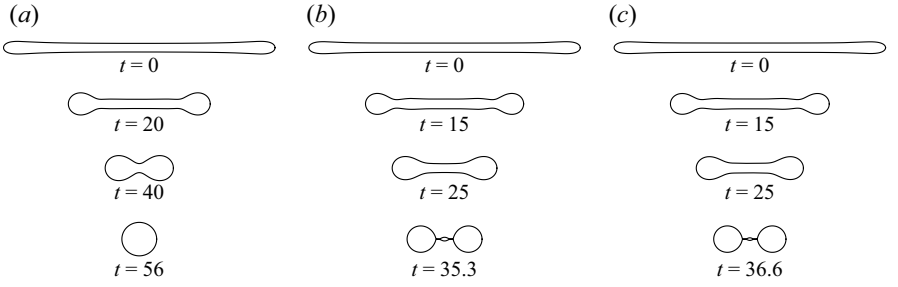

Figure 19. Relaxation of an initially extended droplet in a stagnant fluid for three cases having the same initial shape ($L = 16.0$) over time: (a) droplet with surface shear viscosity ($Bq_\mu = 1$, $Bq_\kappa = 0$), (b) clean droplet ($Bq_\mu = 0$, $Bq_\kappa = 0$) and (c) droplet with surface dilational viscosity ($Bq_\mu = 0$, $Bq_\kappa = 1$). The values of dimensionless parameters are: $\lambda = 1$, $E = 2$, $\Gamma_\infty = 2$ and $\gamma = 1$.

The non-dimensional parameter $\gamma = R'\sigma'_{eq}/D'_s\eta'$ in the above equation denotes the ratio of diffusive time scale R'^2/D'_s to capillary time scale $R'\eta'/\sigma'_{eq}$.

Figure 18 shows the droplet relaxation of an initially extended droplet with initial length $L = 16$ for three cases: droplet with only surface shear viscosity ($Bq_\mu = 1, Bq_\kappa = 0$), clean droplet ($Bq_\mu = 0$, $Bq_\kappa = 0$) and droplet with only surface dilational viscosity ($Bq_\mu = 0$, $Bq_\kappa = 1$). The values of dimensionless parameters are: $\lambda = 1$, $E = 0.2$, $\Gamma_\infty = 2$ and $\gamma = 1.0$. As we can see, both clean droplet and droplet with surface dilational viscosity eventually break up by an end-pinching mechanism. In the case of the droplet with surface shear viscosity, the droplet becomes stable and eventually returns to a spherical shape.

In the next example shown in figure 19, we keep all the parameters the same as in figure 18 but increase the E from 0.2 to 2. At $E = 2$, the higher sensitivity of surface tension to surfactant concentration enhances the Marangoni stresses and reduces the effective surface tension. As a result of these two effects, the initial shapes at $E = 2$ have less pronounced bulging ends than the initial droplet shapes shown at $E = 0.2$ in figure 18. Here also, we observe that the droplet with surface shear viscosity eventually returns to a spherical shape. In the case of clean droplet and droplet with only surface dilational viscosity, the droplet breaks into two smaller droplets.

In figure 20, we examine the relaxation of a droplet with very low viscosity ratio $\lambda = 0.01$ and initial extension $L = 10$ for three cases: a clean droplet ($Bq_\mu = 0$, $Bq_\kappa = 0$), a droplet with equal surface viscosity ($Bq = 0.4$, $\lambda_{ds} = 1$) and a droplet with only surface shear viscosity ($Bq = 0.4$, $\lambda_{ds} = 0$). The values of dimensionless parameters are:

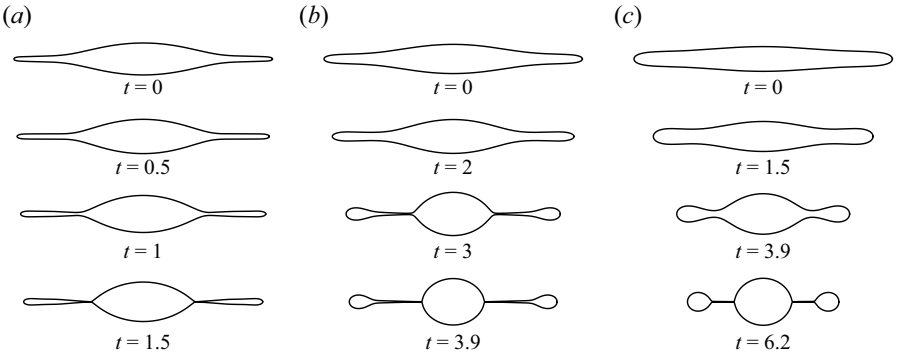

Figure 20. Relaxation of an initially extended droplet in a stagnant fluid for three cases having the same initial shape ($L = 10.0$) over time: (a) clean droplet ($Bq_\mu = 0$, $Bq_\kappa = 0$), (b) droplet with equal surface viscosity ($Bq_\mu = 0.2$, $Bq_\kappa = 0.2$) and (c) droplet with only surface shear viscosity ($Bq_\mu = 0.4$, $Bq_\kappa = 0.0$). The values of dimensionless parameters are: $\lambda = 0.01$, $E = 2$, $\Gamma_\infty = 2$ and $\gamma = 1$.

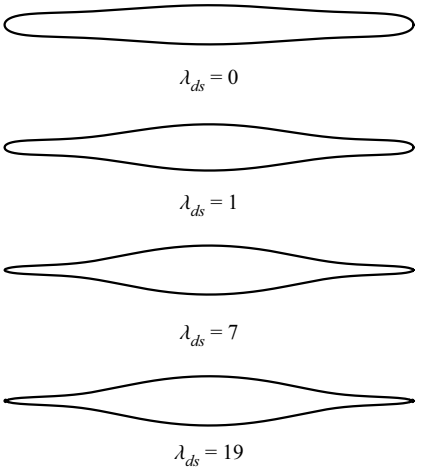

Figure 21. Droplet shapes at different values of λ_{ds} having the same axial extension $L = 10$. The values of dimensionless parameters are: $\lambda = 0.01$, $Bq = 0.4$, $E = 2$, $\Gamma_\infty = 2$ and $\gamma = 1$.

$E = 2$, $\Gamma_\infty = 2$ and $\gamma = 1.0$. We observe that the clean droplet becomes unstable with the eventual breaking of the thin filaments from the droplet's poles. In the case of a droplet with surface viscosity (figure 20b,c), the middle portion of the droplet gradually reduces to an almost spherical shape. The droplet's poles form very small droplets that appear to pinch off from the parent droplet at times $t = 3.9$ and $t = 6.2$, respectively. We observe that the droplet with surface viscosity has a higher breakup time than the clean droplet. Figure 21 shows droplet shapes at different values of λ_{ds} having the same axial extension $L = 10$. The values of dimensionless parameters are: $\lambda = 0.01$, $Bq = 0.4$, $E = 2$, $\Gamma_\infty = 2$ and $\gamma = 1$. We see that droplets with a higher value of interfacial viscosity ratio λ_{ds} have more pronounced pointed ends than droplets with a lower value of λ_{ds}. At higher values of interfacial viscosity ratio $\lambda_{ds} > 7$, the droplet breakup under relaxation will be similar to that of a clean droplet.

In figure 22, we examine the relaxation of a droplet with viscosity ratio $\lambda = 0.05$ and initial extension $L = 10$ for four cases: droplet with surface shear viscosity ($\lambda_{ds} = 0$) and

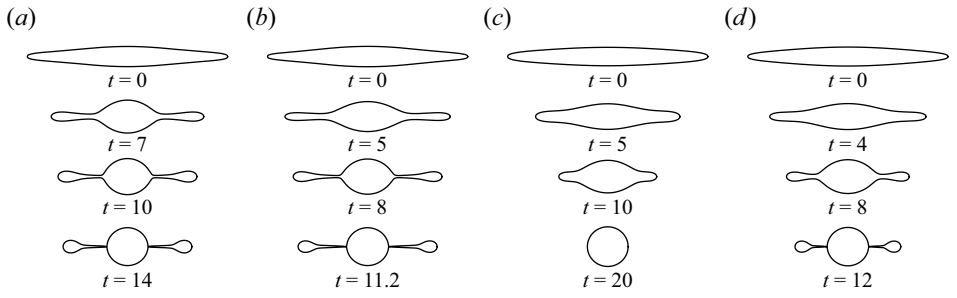

Figure 22. Relaxation of an initially extended droplet in a stagnant fluid for four cases having the same initial shape ($L = 10.0$) over time: (*a*) droplet with surface shear viscosity ($\lambda_{ds} = 0$) and $E = 0.4$, (*b*) droplet with equal surface viscosity ($\lambda_{ds} = 1$) and $E = 0.4$, (*c*) droplet with surface shear viscosity ($\lambda_{ds} = 0$) and $E = 2.0$ and (*d*) droplet with equal surface viscosity ($\lambda_{ds} = 1$) and $E = 2.0$. The values of dimensionless parameters are: $\lambda = 0.05$, $Bq = 0.4$, $\Gamma_\infty = 2$ and $\gamma = 100$.

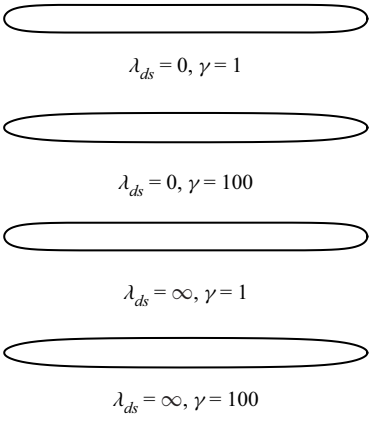

Figure 23. Droplet shapes at different combinations of λ_{ds} and γ with the same axial extension $L = 10$. The values of dimensionless parameters are: $\lambda = 10$, $Bq = 0.4$, $E = 0.4$ and $\Gamma_\infty = 2$.

$E = 0.4$, droplet with equal surface viscosity ($\lambda_{ds} = 1$) and $E = 0.4$, droplet with surface shear viscosity ($\lambda_{ds} = 0$) and $E = 2.0$ and droplet with equal surface viscosity ($\lambda_{ds} = 1$) and $E = 2.0$. The values of dimensionless parameters are: $\lambda = 0.05$, $Bq = 0.4$, $\Gamma_\infty = 2$ and $\gamma = 100$. At $E = 0.4$, the droplet with only surface shear viscosity ($\lambda_{ds} = 0$) and the droplet with equal viscosity ($\lambda_{ds} = 1$) form very small droplets at the poles that appear to pinch off from the parent droplet at times $t = 14$ and $t = 11.2$, respectively. At $E = 2$, the droplet with only surface shear viscosity gradually relaxes into a spherical shape while the droplet with equal surface viscosity breaks and forms daughter droplets at the poles.

Figure 23 shows droplet shapes at different combinations of λ_{ds} and γ with the same axial extension $L = 10$. The values of dimensionless parameters are: $\lambda = 10$, $Bq = 0.4$, $E = 0.4$ and $\Gamma_\infty = 2$. At a higher value of viscosity ratio $\lambda = 10$, the droplet shapes at different values of λ_{ds} are similar for the same initial axial extension and γ value. Droplet shapes at $\gamma = 100$ form pointed ends due to stronger convection of surfactant towards the droplet's ends. We see that irrespective of the interfacial viscosity ratio λ_{ds} and γ values, the droplet eventually returns to a spherical shape. The relaxation of a droplet with $\lambda_{ds} = \infty$ and $\gamma = 100$ is shown in figure 24.

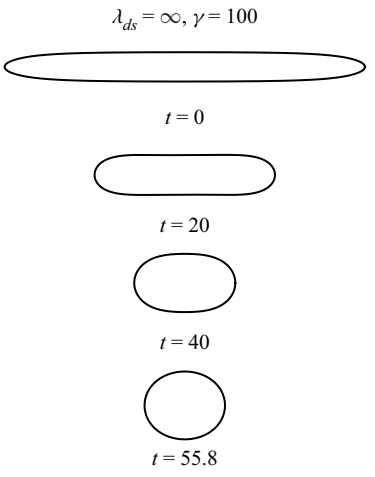

Figure 24. Relaxation of an initially extended droplet with surface dilational viscosity ($\lambda_{ds} = \infty, Bq = 0.4$) and viscosity ratio $\lambda = 10$ in a stagnant fluid with initial shape $L = 10.0$ over time. The values of dimensionless parameters are: $E = 0.4$, $\Gamma_\infty = 2$ and $\gamma = 100$.

5. Conclusion

In this paper, we numerically investigated the effect of surface shear and dilational viscosity on single-droplet dynamics in an axisymmetric domain under the Stokes flow regime. We modelled the droplet rheology using the Boussinesq–Scriven constitutive relationship. We examined how the interfacial viscosity alters the steady-state deformation and the critical capillary number for droplet breakup under uniaxial extensional flow at different values of the droplet's viscosity ratio and surfactant transport parameters. We also discussed the impact of surface viscosity on the relaxation dynamics of an initially extended droplet in a stagnant external fluid.

In the case of a droplet with constant surface viscosity, we found that our numerical results for the Taylor deformation parameter are in good quantitative agreement with second-order perturbation theories up to $O(Ca^2)$. The critical capillary numbers from our boundary-element analysis are found to be within 15 % of the theoretical results. Similar correlations have been reported in previous literature examining clean droplet deformation and breakup under extensional flow (Rallison & Acrivos 1978). We observed that the surface shear/dilational viscosity increases/decreases the critical capillary number for droplet breakup by reducing/increasing the droplet deformation at a given capillary number and viscosity ratio compared with a clean droplet. We found that the isolated effect of surface viscosity increases the steady-state droplet deformation compared with a clean droplet for droplets with $\lambda_{ds} > O(1)$. This will be the case for the majority of surfactant systems as the experimentally reported values of surface dilational viscosity are reported to be several orders of magnitude higher than the surface shear viscosity (Krägel *et al.* 1996; Erni *et al.* 2003; Freer *et al.* 2004; Erni *et al.* 2011; Kim *et al.* 2011; Verwijlen *et al.* 2013; Samaniuk & Vermant 2014; Xiong *et al.* 2018).

We also discussed the combined influence of surface viscosity and surfactant transport on droplet deformation and breakup. We incorporated the effect of surfactant transport by assuming the Langmuir equation of state to correlate interfacial tension with surfactant concentration changes. We observed that the critical capillary number decreases upon increasing the interfacial viscosity ratio λ_{ds} at different values of surface Péclet number.

	Pressure-thinning	Pressure-thickening
$Pe_s = 0.01$	Lower	Higher
$Pe_s = 10$	Lower	Higher

Table 4. Changes in Taylor deformation parameter D_{Taylor} of a droplet with pressure-dependent surface shear viscosity relative to the pressure-independent case.

	Pressure-thinning	Pressure-thickening
$Pe_s = 0.01$	Higher	Lower
$Pe_s = 10$	Lower	Higher

Table 5. Changes in Taylor deformation parameter D_{Taylor} of a droplet with pressure-dependent surface dilational viscosity relative to the pressure-independent case.

At high values of surface Péclet number, the Marangoni effects dominate over the effect of interfacial viscosities and Ca_C of a droplet with surface viscosity is found to be the same as that of a clean droplet. We investigated the effect of Π-thickening and Π-thinning surfactants on droplet deformation and breakup by assuming an exponential dependence of surface viscosity on surface pressure. For a droplet with surface shear viscosity, at both low and high values of surface Péclet number, we observed that droplets with pressure-thinning/thickening surfactant have higher/lower Ca_C than droplets with pressure-independent surfactant. However, the effect of surface viscosity on Ca_C is not very pronounced at $Pe_s = 10$. In contrast, for a droplet with surface dilational viscosity, at a low value of Pe_s, a droplet with pressure-thinning/thickening surfactant has lower/higher Ca_C compared with a droplet with pressure-independent surfactant. For a droplet with surface dilational viscosity, at a high value of Pe_s, a droplet with Π-thickening surfactant is observed to be only slightly more deformed than a droplet with Π-thinning surfactant, and we do not observe a significant difference in Ca_C. Tables 4 and 5 summarize how the Taylor deformation parameter results for a droplet with pressure-dependent surface shear and dilational viscosity differ from those for the pressure-independent case, respectively.

We also discussed the influence of interfacial viscosity on the relaxation of an initially extended droplet in a quiescent fluid at different values of droplet viscosity ratio λ (0.01, 0.05, 1 and 10), elasticity number E (0.2, 0.4 and 2) and surfactant parameter γ (1 and 100) that denotes the ratio of diffusive time scale to capillary time scale. At a low value of $\lambda = 0.01$, a droplet with surface viscosity eventually breaks and forms daughter droplets irrespective of the interfacial viscosity ratio. In contrast, at a high value of λ, a droplet with surface viscosity relaxes into a stable spherical shape irrespective of the interfacial viscosity ratio. At a moderate value of $\lambda = 1$, we observe that surface dilational viscosity aids in end pinching while surface shear viscosity suppresses the effect, and the droplet relaxes into a stable spherical shape. In cases where a droplet with surface viscosity breaks under relaxation, we observe that the droplet takes a longer time to pinch off compared with a clean droplet. We observe that a high value of elasticity number $E = 2$ suppresses/delays the pinch-off compared to low values of elasticity number ($E = 0.2$ and $E = 0.4$).

Acknowledgements. The authors would like to thank the Michael and Carolyn Ott Endowment of Purdue University.

Declaration of interests. The authors report no conflict of interest.

Author ORCIDs.
Vivek Narsimhan https://orcid.org/0000-0001-7448-4202.

References

Acrivos, A. & Lo, T.S. 1978 Deformation and breakup of a single slender drop in an extensional flow. *J. Fluid Mech.* **86** (4), 641–672.

Balemans, C., Hulsen, M.A. & Anderson, P.D. 2016 Modeling of complex interfaces for pendant drop experiments. *Rheol. Acta* **55** (10), 801–822.

Barthès-Biesel, D. 2009 Capsule motion in flow: deformation and membrane buckling. *C. R. Phys.* **10** (8), 764–774.

Barthes-Biesel, D. & Acrivos, A. 1973 Deformation and burst of a liquid droplet freely suspended in a linear shear field. *J. Fluid Mech.* **61** (1), 1–22.

Belyaeva, E., Della Valle, D., Neufeld, R.J. & Poncelet, D. 2004 New approach to the formulation of hydrogel beads by emulsification/thermal gelation using a static mixer. *Chem. Engng Sci.* **59** (14), 2913–2920.

Bentley, B.J. & Leal, L.G. 1986 An experimental investigation of drop deformation and breakup in steady, two-dimensional linear flows. *J. Fluid Mech.* **167**, 241–283.

Boussinesq, M.J. 1913 Sur l'existence d'une viscosité superficielle, dans la mince couche de transition séparant un liquide d'un autre fluide contigu. *Ann. Chim. Phys.* **29**, 349–357.

Brooks, C.F., Fuller, G.G., Frank, C.W. & Robertson, C.R. 1999 An interfacial stress rheometer to study rheological transitions in monolayers at the air-water interface. *Langmuir* **15** (7), 2450–2459.

Chang, K.-S. & Olbricht, W.L. 1993 Experimental studies of the deformation and breakup of a synthetic capsule in steady and unsteady simple shear flow. *J. Fluid Mech.* **250**, 609–633.

Choi, S.Q., Steltenkamp, S., Zasadzinski, J.A. & Squires, T.M. 2011 Active microrheology and simultaneous visualization of sheared phospholipid monolayers. *Nat. Commun.* **2** (1), 1–6.

Cox, R.G. 1969 The deformation of a drop in a general time-dependent fluid flow. *J. Fluid Mech.* **37** (3), 601–623.

Daly, R., Harrington, T.S., Martin, G.D. & Hutchings, I.M. 2015 Inkjet printing for pharmaceutics – a review of research and manufacturing. *Intl J. Pharm.* **494** (2), 554–567.

Dan, A., Gochev, G., Krägel, J., Aksenenko, E.V., Fainerman, V.B. & Miller, R. 2013 Interfacial rheology of mixed layers of food proteins and surfactants. *Curr. Opin. Colloid Interface Sci.* **18** (4), 302–310.

Erni, P. 2011 Deformation modes of complex fluid interfaces. *Soft Matt.* **7** (17), 7586–7600.

Erni, P., Fischer, P., Windhab, E.J., Kusnezov, V., Stettin, H. & Läuger, J. 2003 Stress-and strain-controlled measurements of interfacial shear viscosity and viscoelasticity at liquid/liquid and gas/liquid interfaces. *Rev. Sci. Instrum.* **74** (11), 4916–4924.

Erni, P., Windhab, E.J. & Fischer, P. 2011 Emulsion drops with complex interfaces: globular versus flexible proteins. *Macromol. Mater. Engng* **296** (3–4), 249–262.

Feigl, K., Megias-Alguacil, D., Fischer, P. & Windhab, E.J. 2007 Simulation and experiments of droplet deformation and orientation in simple shear flow with surfactants. *Chem. Engng Sci.* **62** (12), 3242–3258.

Flumerfelt, R.W. 1980 Effects of dynamic interfacial properties on drop deformation and orientation in shear and extensional flow fields. *J. Colloid Interface Sci.* **76** (2), 330–349.

Frankel, N.A. & Acrivos, A. 1970 The constitutive equation for a dilute emulsion. *J. Fluid Mech.* **44** (1), 65–78.

Freer, E.M., Yim, K.S., Fuller, G.G. & Radke, C.J. 2004 Shear and dilatational relaxation mechanisms of globular and flexible proteins at the hexadecane/water interface. *Langmuir* **20** (23), 10159–10167.

Fuller, G.G. & Vermant, J. 2012 Complex fluid-fluid interfaces: rheology and structure. *Annu. Rev. Chem. Biomol. Engng* **3**, 519–543.

Georgieva, D., Schmitt, V., Leal-Calderon, F. & Langevin, D. 2009 On the possible role of surface elasticity in emulsion stability. *Langmuir* **25** (10), 5565–5573.

Gounley, J., Boedec, G., Jaeger, M. & Leonetti, M. 2016 Influence of surface viscosity on droplets in shear flow. *J. Fluid Mech.* **791**, 464–494.

Gunning, A.P., Kirby, A.R., Wilde, P.J., Penfold, R., Woodward, N.C. & Morris, V.J. 2013 Probing the role of interfacial rheology in the relaxation behaviour between deformable oil droplets using force spectroscopy. *Soft Matt.* **9** (48), 11473–11479.

HAMED, R., SCHENCK, D.M. & FIEGEL, J. 2020 Surface rheological properties alter aerosol formation from mucus mimetic surfaces. *Soft Matt.* **16** (33), 7823–7834.

HE, B., YANG, S., QIN, Z., WEN, B. & ZHANG, C. 2017 The roles of wettability and surface tension in droplet formation during inkjet printing. *Sci. Rep.* **7** (1), 1–7.

HERMANS, E. & VERMANT, J. 2014 Interfacial shear rheology of dppc under physiologically relevant conditions. *Soft Matt.* **10** (1), 175–186.

HERRADA, M.A., PONCE-TORRES, A., RUBIO, M., EGGERS, J. & MONTANERO, J.M. 2022 Stability and tip streaming of a surfactant-loaded drop in an extensional flow, influence of surface viscosity. *J. Fluid Mech.* **934**, A26.

HINCH, E.J. & ACRIVOS, A. 1979 Steady long slender droplets in two-dimensional straining motion. *J. Fluid Mech.* **91** (3), 401–414.

HINCH, E.J. & ACRIVOS, A. 1980 Long slender drops in a simple shear flow. *J. Fluid Mech.* **98** (2), 305–328.

JAENSSON, N.O., ANDERSON, P.D. & VERMANT, J. 2021 Computational interfacial rheology. *J. Non-Newtonian Fluid Mech.* **290**, 104507.

KAMAT, P.M., WAGONER, B.W., THETE, S.S. & BASARAN, O.A. 2018 Role of Marangoni stress during breakup of surfactant-covered liquid threads: reduced rates of thinning and microthread cascades. *Phys. Rev. Fluids* **3** (4), 043602.

VAN KEMPEN, S.E.H.J., SCHOLS, H.A., VAN DER LINDEN, E. & SAGIS, L.M.C. 2013 Non-linear surface dilatational rheology as a tool for understanding microstructures of air/water interfaces stabilized by oligofructose fatty acid esters. *Soft Matt.* **9** (40), 9579–9592.

KENNEDY, M.R., POZRIKIDIS, C. & SKALAK, R. 1994 Motion and deformation of liquid drops, and the rheology of dilute emulsions in simple shear flow. *Comput. Fluids* **23** (2), 251–278.

KIM, K., CHOI, S.Q., ZASADZINSKI, J.A. & SQUIRES, T.M. 2011 Interfacial microrheology of DPPC monolayers at the air–water interface. *Soft Matt.* **7** (17), 7782–7789.

KIM, K., CHOI, S.Q., ZELL, Z.A., SQUIRES, T.M. & ZASADZINSKI, J.A. 2013 Effect of cholesterol nanodomains on monolayer morphology and dynamics. *Proc. Natl Acad. Sci. USA* **110** (33), E3054–E3060.

KRÄGEL, J., KRETZSCHMAR, G., LI, J.B., LOGLIO, G., MILLER, R. & MÖHWALD, H. 1996 Surface rheology of monolayers. *Thin Solid Films* **284**, 361–364.

KURTZ, R.E., LANGE, A. & FULLER, G.G. 2006 Interfacial rheology and structure of straight-chain and branched fatty alcohol mixtures. *Langmuir* **22** (12), 5321–5327.

LAM, S., VELIKOV, K.P. & VELEV, O.D. 2014 Pickering stabilization of foams and emulsions with particles of biological origin. *Curr. Opin. Colloid Interface Sci.* **19** (5), 490–500.

LANGEVIN, D. 2000 Influence of interfacial rheology on foam and emulsion properties. *Adv. Colloid Interface Sci.* **88** (1–2), 209–222.

LEMENAND, T., DUPONT, P., DELLA VALLE, D. & PEERHOSSAINI, H. 2013 Comparative efficiency of shear, elongation and turbulent droplet breakup mechanisms: review and application. *Chem. Engng Res. Des.* **91** (12), 2587–2600.

LI, X.Z., BARTHES-BIESEL, D. & HELMY, A. 1988 Large deformations and burst of a capsule freely suspended in an elongational flow. *J. Fluid Mech.* **187**, 179–196.

LI, X. & POZRIKIDIS, C. 1997 The effect of surfactants on drop deformation and on the rheology of dilute emulsions in Stokes flow. *J. Fluid Mech.* **341**, 165–194.

LUO, Z.Y., SHANG, X.L. & BAI, B.F. 2019 Influence of pressure-dependent surface viscosity on dynamics of surfactant-laden drops in shear flow. *J. Fluid Mech.* **858**, 91–121.

MANIKANTAN, H. & SQUIRES, T.M. 2017 Pressure-dependent surface viscosity and its surprising consequences in interfacial lubrication flows. *Phys. Rev. Fluids* **2** (2), 023301.

MILLER, R., FERRI, J.K., JAVADI, A., KRÄGEL, J., MUCIC, N. & WÜSTNECK, R. 2010 Rheology of interfacial layers. *Colloid Polym. Sci.* **288** (9), 937–950.

MILLIKEN, W.J., STONE, H.A. & LEAL, L.G. 1993 The effect of surfactant on the transient motion of Newtonian drops. *Phys. Fluids* A*: Fluid* **5** (1), 69–79.

NARSIMHAN, G., WANG, Z. & XIANG, N. 2019 Guidelines for processing emulsion-based foods. In *Food Emulsifiers and their Applications* (ed. G.L. Hasenhuettl & R.W. Hartel), pp. 435–501. Springer.

NARSIMHAN, V. 2019 Shape and rheology of droplets with viscous surface moduli. *J. Fluid Mech.* **862**, 385–420.

PAWAR, Y. & STEBE, K.J. 1996 Marangoni effects on drop deformation in an extensional flow: the role of surfactant physical chemistry. I. Insoluble surfactants. *Phys. Fluids* **8** (7), 1738–1751.

POURALI, M., KRÖGER, M., VERMANT, J., ANDERSON, P.D. & JAENSSON, N.O. 2021 Drag on a spherical particle at the air–liquid interface: interplay between compressibility, marangoni flow, and surface viscosities. *Phys. Fluids* **33** (6), 062103.

POZRIKIDIS, C. 1990 The instability of a moving viscous drop. *J. Fluid Mech.* **210**, 1–21.
POZRIKIDIS, C. 1992 *Boundary Integral and Singularity Methods for Linearized Viscous Flow*. Cambridge University Press.
RALLISON, J.M. 1981 A numerical study of the deformation and burst of a viscous drop in general shear flows. *J. Fluid Mech.* **109**, 465–482.
RALLISON, J.M. & ACRIVOS, A. 1978 A numerical study of the deformation and burst of a viscous drop in an extensional flow. *J. Fluid Mech.* **89** (1), 191–200.
SAMANIUK, J.R. & VERMANT, J. 2014 Micro and macrorheology at fluid–fluid interfaces. *Soft Matt.* **10** (36), 7023–7033.
SCRIVEN, L.E. 1960 Dynamics of a fluid interface equation of motion for Newtonian surface fluids. *Chem. Engng Sci.* **12** (2), 98–108.
SHMYROV, A. & MIZEV, A. 2019 Surface diffusion in gaseous monolayers of an insoluble surfactant. *Langmuir* **35** (44), 14180–14187.
SINGH, N. & NARSIMHAN, V. 2020 Deformation and burst of a liquid droplet with viscous surface moduli in a linear flow field. *Phys. Rev. Fluids* **5** (6), 063601.
SINGH, N. & NARSIMHAN, V. 2021 Impact of surface viscosity on the stability of a droplet translating through a stagnant fluid. *J. Fluid Mech.* **927**, A44.
STONE, H.A. 1990 A simple derivation of the time-dependent convective-diffusion equation for surfactant transport along a deforming interface. *Phys. Fluids* A*: Fluid* **2** (1), 111–112.
STONE, H.A., BENTLEY, B.J. & LEAL, L.G. 1986 An experimental study of transient effects in the breakup of viscous drops. *J. Fluid Mech.* **173**, 131–158.
STONE, H.A. & LEAL, L.G. 1990 The effects of surfactants on drop deformation and breakup. *J. Fluid Mech.* **220**, 161–186.
TAYLOR, G.I. 1934 The formation of emulsions in definable fields of flow. *Proc. R. Soc. Lond.* A **146** (858), 501–523.
VERWIJLEN, T., MOLDENAERS, P. & VERMANT, J. 2013 A fixture for interfacial dilatational rheometry using a rotational rheometer. *Eur. Phys. J.: Spec. Top.* **222** (1), 83–97.
VLAHOVSKA, P.M., BŁAWZDZIEWICZ, J. & LOEWENBERG, M. 2009 Small-deformation theory for a surfactant-covered drop in linear flows. *J. Fluid Mech.* **624**, 293–337.
WONG, H., RUMSCHITZKI, D. & MALDARELLI, C. 1996 On the surfactant mass balance at a deforming fluid interface. *Phys. Fluids* **8** (11), 3203–3204.
XIONG, W., REN, C., TIAN, M., YANG, X., LI, J. & LI, B. 2018 Emulsion stability and dilatational viscoelasticity of ovalbumin/chitosan complexes at the oil-in-water interface. *Food Chem.* **252**, 181–188.
ZELL, Z.A., NOWBAHAR, A., MANSARD, V., LEAL, L.G., DESHMUKH, S.S., MECCA, J.M., TUCKER, C.J. & SQUIRES, T.M. 2014 Surface shear inviscidity of soluble surfactants. *Proc. Natl Acad. Sci. USA* **111** (10), 3677–3682.